

## Axial compressive behavior of special-shaped concrete filled tube mega column coupled with multiple cavities

Haipeng Wu<sup>a</sup>, Qiyun Qiao<sup>\*</sup>, Wanlin Cao<sup>b</sup>, Hongying Dong<sup>c</sup> and Jianwei Zhang<sup>d</sup>

College of Architecture and Civil Engineering, Beijing University of Technology,  
100 Ping Le Yuan, Chaoyang District, Beijing, China

(Received June 01, 2015, Revised November 17, 2016, Accepted February 14, 2017)

**Abstract.** The compressive behavior of special-shaped concrete filled tube (CFT) mega column coupled with multiple cavities is studied by testing six columns subjected to cyclically uniaxial compressive load. The six columns include three pentagonal specimens and three hexagonal specimens. The influence of cavity construction, arrangement of reinforcement, concrete strength on failure feature, bearing capacity, stiffness, and residual deformation is examined. Experimental results show that cavity construction and reinforcements make it possible to form a combined confinement effect to in-filled concrete, and the two groups of special-shaped CFT columns show good elastic-plastic compressive behavior. As there is no axial bearing capacity calculation method currently available in any Code of practice for special-shaped CFT columns, values predicted by normal CFT column formulas in GB50936, CECS254, ACI-318, EC4, AISI-LRFD, CECS159, and AIJ are compared with tested values. The calculated values are lower than the tested values for most columns, thus the predicted bearing capacity is safe. A reasonable calculation method by dividing concrete into active and inactive confined regions is proposed. And high accuracy shows in estimating special-shaped CFT columns either coupled with multiple cavities or not. In addition, a finite element method (FEM) analysis is conducted and the simulated results match the test well.

**Keywords:** CFT; mega column; pentagonal; hexagonal; compressive behavior; bearing capacity; FEM analysis

### 1. Introduction

Concrete filled tubes (CFTs) are practical structural members widely used in construction. CFTs combine steel and concrete, resulting in a member that has the beneficial qualities of high tensile strength and ductility of steel and high compressive strength and stiffness of concrete. Compared with reinforced concrete (RC) members, CFTs have the advantage of saving cost for the reason that the lettable floor area is increased while the required structural cross-section area is reduced. It is very important for high-rise buildings in cities where the cost of letting spaces is extremely high. Among the vast used CFTs, circular and rectangular tubular columns are most general. However, in recent years, new shaped tubular columns appear.

Several super high-rise buildings possessing a roof height of more than 400 meters are under construction or have been built in China. Most of them use mega frame-core walls structure as lateral force resisting system (Kim and Kang 2012, Lee *et al.* 2014). Usually mega columns are arranged at the corners of a building to bear giant axial load, and the cross section area may exceed tens of square meters

(m<sup>2</sup>). For instance, Tianjin Goldin 117 mega tower in Fig. 1 has a roof height of 597 m, a structural height of 584 m and an up ground stories of 117, all make it the highest building in earthquake region (0.15 g,  $g = 9.8 \text{ m/s}^2$ ) in the world. In order to meet the requirements of architectural image, cost, structural safety, mass volume concrete, and so on, the mega columns are designed into an irregular hexagonal CFT coupled with multiple cavities with a cross sectional area of 45 m<sup>2</sup>. Although special-shaped CFT columns are suitable for super high-rise buildings in high seismic regions, the application is limited due to a lack of information about the true strength and inelastic behavior.

Only the design methods for circular, square, and regular octagon CFT columns have been written in codes or specifications, such as, Chinese CECS 254 specification (2012) and Chinese GB 50936 (2014) code which are based on 'unified theory', American ACI 318 code (2011) and European Eurocode 4 (2004) which are based on 'quasi concrete theory', American AISI-LRFD specification (1999) which is based on 'quasi steel theory', Chinese CECS 159 specification (2004) and Japanese AIJ standard (2001) which are based on 'superposition theory'. In 'unified theory', the steel tube and concrete can be seen as a holistic material to study and analyze the composited compressive behavior. The composited compressive behavior changes along with physical parameters. But the change process is continuous, and the calculation method is unified. In 'quasi concrete theory', the steel tubes are converted to longitudinal reinforcements around core concrete. In this way, the bearing capacity of CFT column

\*Corresponding author, Ph.D., Lecturer,

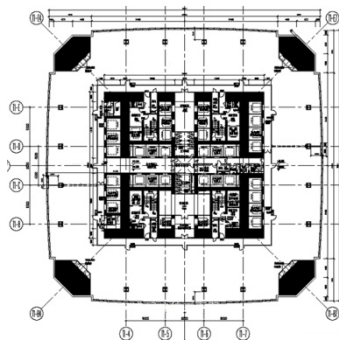
E-mail: [qiaoqiyun@bjut.edu.cn](mailto:qiaoqiyun@bjut.edu.cn)

<sup>a</sup> Ph.D. Student, E-mail: [B201304002@emails.bjut.edu.cn](mailto:B201304002@emails.bjut.edu.cn)

<sup>b</sup> Ph.D., Professor, E-mail: [15201227267@163.com](mailto:15201227267@163.com)

<sup>c</sup> Ph.D., Professor, E-mail: [donghy@bjut.edu.cn](mailto:donghy@bjut.edu.cn)

<sup>d</sup> Ph.D., Professor, E-mail: [zhangjw@bjut.edu.cn](mailto:zhangjw@bjut.edu.cn)



(a) Arrangement of mega columns



(b) Engineering construction site

Fig. 1 Tianjin Goldin 117 mega tower

can be calculated by the use of a reinforced concrete design method. In ‘quasi steel theory’, the concrete material is converted to steel material by increasing yield strength and elastic modulus of steel, and the structural steel design method is used to calculate the bearing capacity. In ‘superposition theory’, the bearing capacity of CFT columns is equal to a sum of steel tube part and core concrete part. The interaction between steel tube and core concrete is excluded.

Experimental research on normal-shaped (circular and rectangular) CFT columns has been conducted worldwide for decades (Hua *et al.* 2014, Chithira and Baskar 2014, Gupta *et al.* 2015). In addition, there have been a few researches about T-shaped, L-shaped, and crisscross-shaped CFT columns mainly in China. However, little attention has been paid to irregular pentagonal and hexagonal CFT columns. Li and Lu (2008) conducted an experiment on L-shaped and T-shaped CFT columns subjected to low cyclic load. Shen *et al.* (2013) conducted an experiment on L-shaped CFT stub columns with stiffen ribs subjected to low cyclic load. Zuo *et al.* (2012) conducted an experiment on T-shaped and L-shaped CFT columns with binding bars under axial load. Du *et al.* (2013) proposed L-shaped CFT stub columns with built-in shape steel and tested axial compressive behavior. Tu *et al.* (2014) studied confinement effect of steel tube on in-filled concrete in T-shaped CFT columns with multiple cavities, modified expression of Mander’s confinement concrete model, and established new constitutive relation of core concrete. Jamaluddin *et al.* (2013) conducted an experiment on elliptical CFT columns under axial compression. Qian *et al.* (2011) conducted an axial compressive experiment of square CFT composite stub columns with inner round steel tube and in-filled high strength concrete, and conducted FEM analysis and ultimate bearing capacity calculation. Li *et al.* (2016) conducted an experimental study on the behavior of a composite FRP-concrete-steel member under bi-axial eccentric loading.

Previous researches show that reasonable designed T-shaped, L-shaped, and crisscross-shaped CFT columns have high bearing capacity and good inelastic deformability. Arrangement of multiple cavities, binding bars, encased shape steel, or encased steel tubes all can effectively improve seismic behavior of special-shaped CFT columns. In this paper, irregular hexagonal and pentagonal CFT mega columns coupled with multiple cavities derived from

Tianjin Goldin 117 mega tower (Liu *et al.* 2012) and Dalian Guomao Tower (Wang *et al.* 2012) were specifically studied. The purpose is to define the bearing capacity, inelastic behavior and failure mode, and then to provide design suggestions.

## 2. Experimental program

### 2.1 Specimens design

A total of six mega column modeling specimens were tested under axial compressive load. They are divided into two groups according to cross section shape. Group ‘H’ includes three hexagonal CFT mega columns coupled with multiple cavities modeling specimens, while group ‘P’ includes three pentagonal CFT mega columns coupled with multiple cavities modeling specimens. The total height of the specimens in each group is 3000 mm. Cuboid loading blocks with a height of 250 mm are arranged at upper end and lower end of each specimen, making it easy to apply axial load uniformly. The main difference between the two groups lies in the cross section shape and multi-cavity construction.

The three 1/12 scaling specimens in group ‘H’ are labeled CFT1-H, CFT2-H, CFT3-H respectively. The steel tube cross sections are the same in geometric dimension. They are welded into a hexagon with six cavities by 5mm Q235 steel plates. In order to enhance co-operative performance between steel plates and in-filled concrete, studs that are 4mm in diameter and 30mm in length are welded to the inner sides of steel plates of each cavity at an interval of 60 mm × 60 mm. The main variable parameters of the three specimens are arrangement of reinforcement in cavities and concrete strength. For CFT1-H, 5 $\phi$ 8, 6 $\phi$ 10 and 5 $\phi$ 12 ( $\phi$  represents diameter) longitudinal reinforcements are arranged and C30 concrete is poured in each cavity. For CFT2-H, no longitudinal reinforcement is arranged and C40 concrete is poured. For CFT3-H, the longitudinal reinforcement arrangement is the same with that of CFT1-H, and C40 concrete is poured. The main parameters and running parameters are listed in Table 1 and the construction details are shown in Fig. 2.

The three 1/5 scaling specimens in group ‘P’ are labeled CFT1-P, CFT2-P, CFT3-P respectively. The external steel

Table 1 Main parameters

Shape	Specimens	$A/\text{mm}^2$	$f_{cu,m}/\text{MPa}$	$\bar{f}_y/\text{MPa}$	$\rho_1/\%$	$\rho_2/\%$	$\xi$
Hexagon	CFT1-H		30.68	300.5		0.82	0.947
	CFT2-H	313094	41.97	295.0	6.02	0	0.592
	CFT3-H			300.5	0.82	0.692	
Pentagon	CFT1-P			378.5	9.49	0.29	1.056
	CFT2-P	354016	51.11	385.8	11.41	0	1.297
	CFT3-P			385.7	11.41	0.29	1.333

\*Note:  $A$  is cross section area;  $f_{c,m}$  is average value of concrete axial compressive strength, for prism  $f_{c,m} = 0.76f_{cu,m}$ , and for cylinder  $f_{c,m} = 0.80f_{cu,m}$  (Guo and Shi 2015);  $f_{cu,m}$  is average value of concrete cubic compressive strength;  $\rho_1$  is steel plate ratio;  $\rho_2$  is reinforcement ratio.  $\bar{f}_y$  is equivalent yield strength of steel tube,  $\bar{f}_y = \frac{\sum A_{s1}f_{y1} + \sum A_{s2}f_{y2}}{\sum A_{s1} + \sum A_{s2}}$ ;  $\xi$  is confinement coefficient,

$\xi = \frac{\sum A_{s1}f_{y1} + \sum A_{s2}f_{y2}}{A_c f_{c,m}}$ ;  $A_{s1}$ ,  $A_{s2}$  are cross section area of steel plate and reinforcement respectively;  $f_{y1}$ ,  $f_{y2}$  are tested yield strength of steel plate and reinforcement respectively;  $A_c$  is net cross section area of concrete

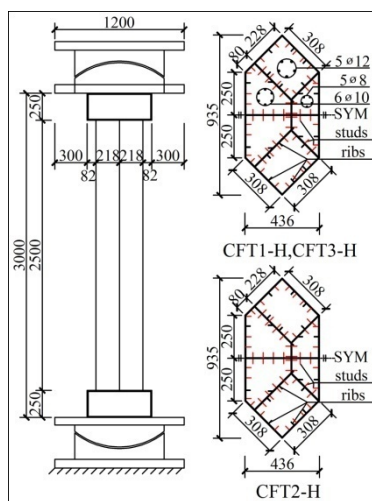


Fig. 2 Specimen design of group 'H' (unit mm)

tube cross sections are the same in geometric dimension. They are welded into a pentagon by 12 mm Q345 steel plates. To improve stability of the external steel tubes, vertical stiffening ribs whose cross sections are 90 mm × 6 mm are welded to the inner sides of external steel tubes, while five-storey horizontal stiffening ribs are welded at a vertical interval of 500 mm. The main variable parameters are arrangement of reinforcement in cavities and multi-cavity construction. For CFT1-P, 13φ10 longitudinal reinforcements are arranged and only one cavity forms. For CFT2-P, no longitudinal reinforcement is arranged and four cavities form. The cross section of CFT2-P is divided into two cavities by a 10 mm thick solid steel plate; and then the cross section is divided into four cavities by two symmetrical 6 mm thick latticed steel plates, on which

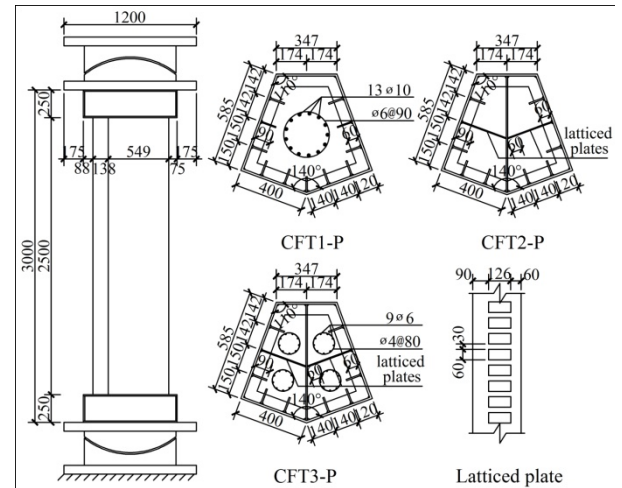


Fig. 3 Specimen design of group 'P' (unit mm)

rectangular holes are punched for the flow of concrete between adjacent cavities. For CFT3-P, based on specimen CFT2-P, 9φ6 longitudinal reinforcements are additionally arranged in each cavity. The main parameters and running parameters are listed in Table 1 and the construction details are shown in Fig. 3.

## 2.2 Material properties

Concrete was poured in two batches in the hexagonal specimens while once in the pentagonal specimens. The strength is determined by standard cubic blocks (150 mm × 150 mm × 150 mm) according to Chinese specification GB/T 50081 (2011). For C30 concrete, the tested average value of cubic compressive strength  $f_{cu,m}$  is 30.68 MPa; for C40 concrete, it is 41.97 MPa; for C50 concrete, it is 51.11 MPa.

Steel mechanical properties are tested according to the standard method in Chinese specification GB/T 228.1 (2010). The tested yield strength, ultimate strength, tensile elongation and elasticity modulus of reinforcements and steel plates are summarized in Table 2.

## 2.3 Test set up

A 40000 kN universal testing machine was used to conduct the axial compressive test. On the upper and lower end of the loading device, spherical hinges are arranged. In test procedure, a cyclic uniaxial load is applied to the specimens to study residual deformation each time the unloading is finished. To prevent overturn of the specimens, the device is unloaded to 2000 kN. In the initial stage (e.g., elastic stage), the specimens are loaded at an interval of 1/6 calculated ultimate load; after evident yielding appears on the load-displacement curves, the loading process turns to be controlled by displacement.

Two displacement meters measuring vertical displacement are arranged in the central 1600 mm gauge length, where the deformation is uniform. Strain gages measuring longitudinal deformation are placed on the outside face of steel plates at central part of steel tubes. Real-time values of load, displacement and strain are gathered by an IMP data

Table 2 Mechanical properties of reinforcements and steel plates

Shape	Steel plates & reinforcements	Location	$f_y$ (MPa)	$f_u$ (MPa)	$\theta$ (%)	$E_s$ (MPa)
Hexagon	5 mm steel plate	Steel tube	296	428	28.9	$2.06 \times 10^5$
	$\phi 8$ reinforcement	Longitudinal reinforcement	334	445	24.5	$2.05 \times 10^5$
	$\phi 10$ reinforcement	Longitudinal reinforcement	363	446	26.3	$2.07 \times 10^5$
	$\phi 12$ reinforcement	Longitudinal reinforcement	326	423	27.1	$2.04 \times 10^5$
Pentagon	6 mm steel plate	Vertical and horizontal stiffening rib, latticed steel plate	416	528	27.5	$2.10 \times 10^5$
	10 mm steel plate	Solid steel plate	409	498	27.6	$2.12 \times 10^5$
	12 mm steel plate	External steel tube	373	525	27.4	$2.06 \times 10^5$
	$\phi 6$ reinforcement	Longitudinal reinforcement	382	582	31.3	$2.07 \times 10^5$
	$\phi 10$ reinforcement	Longitudinal reinforcement	310	473	36.7	$2.05 \times 10^5$

\*Note:  $f_y$  is tested yield strength;  $f_u$  is tested ultimate strength;  $\theta$  is tested tensile elongation;  $E_s$  is tested elastic modulus of steel



Fig. 4 Test scene

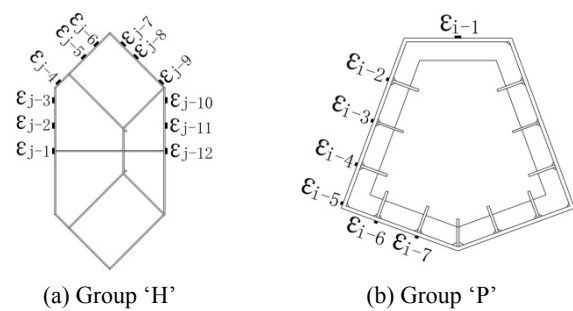


Fig. 6 Strain gages arrangement

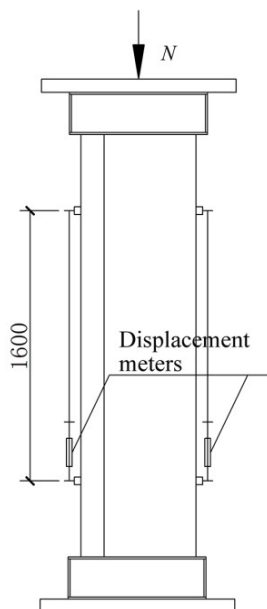


Fig. 5 Displacement meter arrangement

gathering system; the local buckling of external steel tube and crack of welding seams are recorded manually. The test scene photo is shown in Fig. 4; the arrangement of displacement meters is shown in Fig. 5; the distribution of the strain gages is shown in Fig. 6.

### 3. Experimental results

#### 3.1 Test phenomenon

The specimens go through similar failure process. The final failure patterns are shown in Fig. 7. The failure process is characterized in that before the specimens are loaded to 70%~90% of ultimate bearing capacity, the phenomenon is not obvious; when the specimens are loaded to ultimate bearing capacity, wrinkling of oil paint skin appears and the steel plates slightly buckle; with application of axial load, the oil paint skin cracks to drop, and the steel plates of external steel tubes buckle obviously; when the average strain converted by displacement meters in 1600 mm gauge length exceeds three times of steel plate yield strain, the corner weld seam cracks slightly; then the cracks extend and the concrete is compressed to break; finally shear slip plane or global buckling forms and the specimens are damaged. The difference lies in appearance of significant process points. For group 'H' specimens, the damage process of CFT1-H develops fastest, while that of CFT3-H develops slowest. For group 'P' specimens, CFT1-P develops fastest, CFT2-P takes the second place, and CFT3-P develops slowest.

Contrastive analysis. (1) The damage process of group 'P' specimen develops relatively slowly as for relatively higher steel ratio. (2) The wrinkles of oil paint skin of the steel plates of external steel tubes in group 'H' specimens are 45-degree staggered cracks while those in group 'P' specimens are horizontal cracks. (3) The local buckling regions of group 'H' specimens are numerous and scattered,

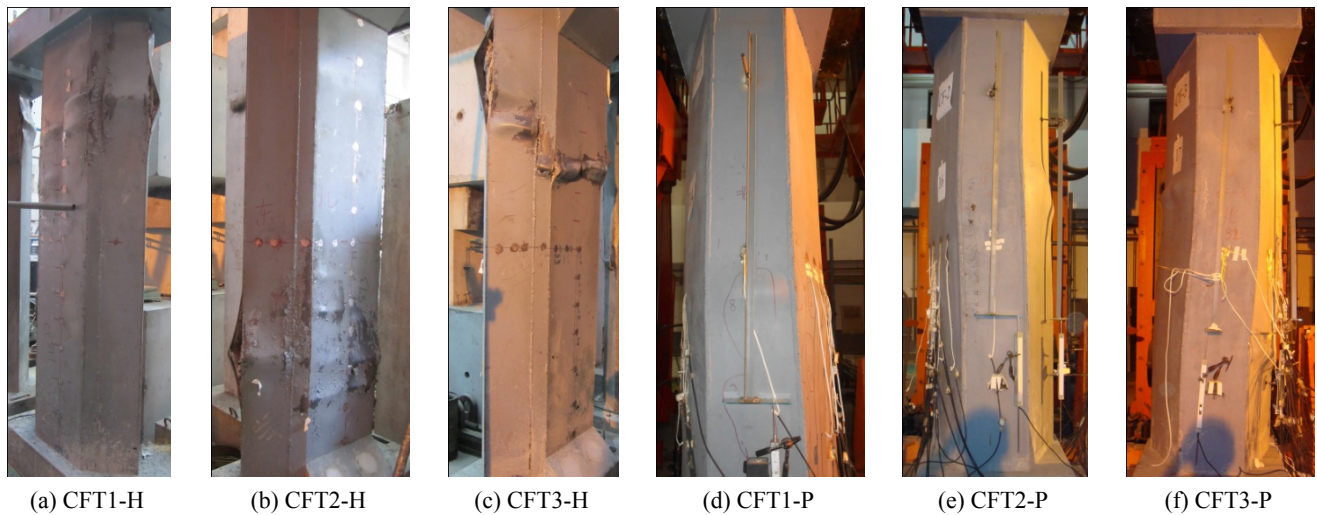


Fig. 7 Failure pattern of specimens

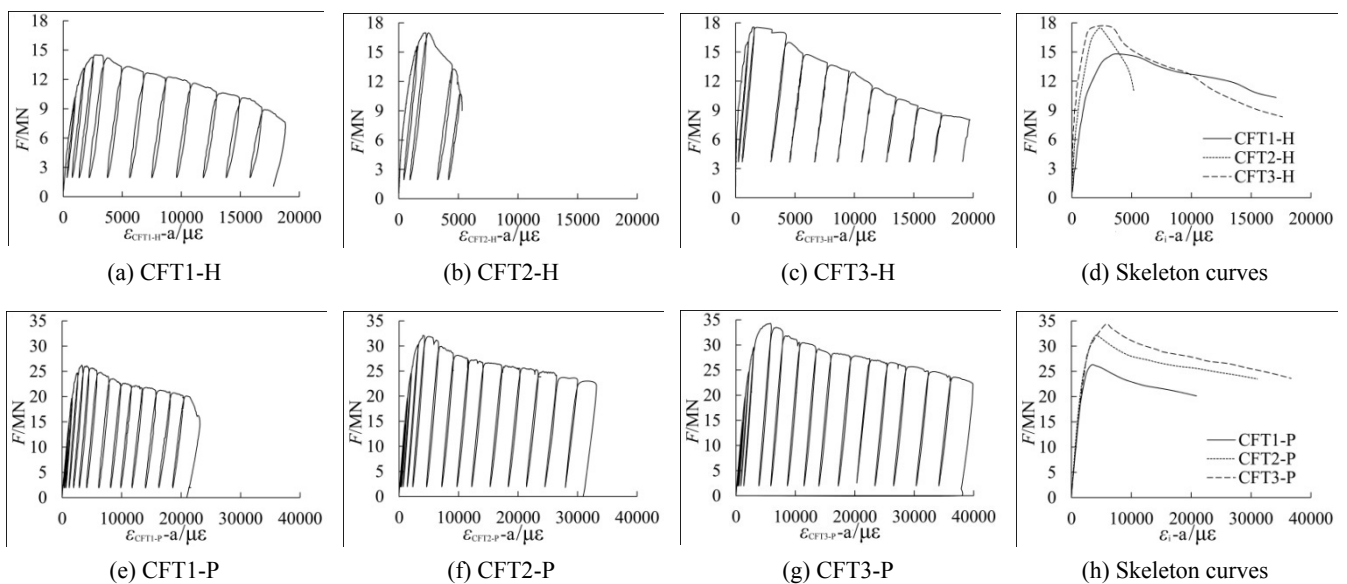


Fig. 8 Axial load ‘ $F$ ’ - average strain ‘ $\varepsilon_i$ -a’ curves

Table 3 Experimental results of characteristic load

Specimens	CFT1-H	CFT2-H	CFT3-H	CFT1-P	CFT2-P	CFT3-P
$F_y$ /kN	12002	15143	15136	20234	24689	26514
$F_u$ /kN	14800	17400	17557	26233	32119	33496
$F_{ud}$ /kN	13238	14946	15741	25504	27940	28285
$\varepsilon_u$ /με	3721	2493	3266	3316	4049	5650
$F_y/F_u$	0.811	0.870	0.862	0.771	0.769	0.774

\*Note:  $F_y$  is yield load;  $F_u$  is ultimate load;  $F_{ud}$  is bearing capacity superposition value of concrete part and steel part;  $F_y/F_u$  is yield ratio;  $\varepsilon_u$  is average strain corresponding to ultimate load

### 3.2 Load-average strain curves

The tested axial load ‘ $F$ ’- average strain ‘ $\varepsilon_i$ -a’ ( $i = \text{CFT1-H} \sim \text{CFT3-H}$ ,  $\text{CFT1-P} \sim \text{CFT3-P}$ ) curves and related skeleton curves are shown in Fig. 8. In Fig. 8, ‘ $F$ ’ represents applied axial load, and ‘ $\varepsilon_i$ -a’ represents average strain converted by the two displacements in 1600 mm gauge length. The tested characteristic loads are shown in Table 3.

It can be known from Fig. 8 and Table 3 that in initial loading stage, the ‘ $F$ -( $\varepsilon_i$ -a)’ curves are linear and the residual deformation is very small after unloading; after the specimens yield, the stiffness degrades gradually and the residual deformation increases; after the axial load reaches ultimate load, the applied load decreases along with the increase of vertical displacement. The ‘ $F$ -( $\varepsilon_i$ -a)’ curves of CFT3-H and CFT1-H are the same in shape, but the yield load and ultimate load of CFT3-H are higher by 26.1% and 18.6% respectively. Compared with CFT2-H, longitudinal reinforcements are additionally arranged in cavities of

but each local buckling region is small and protruding. In contrast, the local buckling regions of group ‘P’ specimens are few and concentrated in only 2 to 3 regions, but each buckling region is large.

CFT3-H; although their yield load and ultimate load are near, the average strain corresponding to ultimate load of CFT3-H is higher by 31% and the inelastic deformability is better. The ‘ $F-(\epsilon_r-a)$ ’ curves of group ‘P’ specimens are the same in shape. Compared with CFT1-P with only one cavity, the ultimate loads of CFT2-P and CFT3-P with four cavities are higher by 22.4%, 27.7% respectively, while the average strains corresponding to ultimate load are higher by 22.1%, 70.4% respectively. Compared with CFT2-P without reinforcement, the ultimate load of CFT3-P with build-in longitudinal reinforcement is higher by 5.3%, while the strain corresponding to the ultimate load is higher by 39.5%.

Contrastive analysis. (1) The higher concrete strength is, the higher bearing capacity of the column is, and the faster the bearing capacity degrades after ultimate load reaches. (2) Multi-cavity construction has a great effect on the bearing capacity and inelastic deformability. The increasing proportion of bearing capacity and inelastic deformability is higher than that of the steel ratio, because of the double confinement effect of external steel tube and inner steel plates on in-filled concrete.

### 3.3 Residual deformation

The tested relative residual deformation ‘ $U_p$ ’-average strain ‘ $\epsilon_r-a$ ’ curves are shown in Fig. 9. In the figure, the vertical coordinate ‘ $U_p$ ’ represents the ratio of plastic deformation acquired when unloading is finished to maximum deformation in each loading cycle; the horizontal coordinate ‘ $\epsilon_r-a$ ’ represents the average strain corresponding to maximum displacement in the loading cycle. The relative

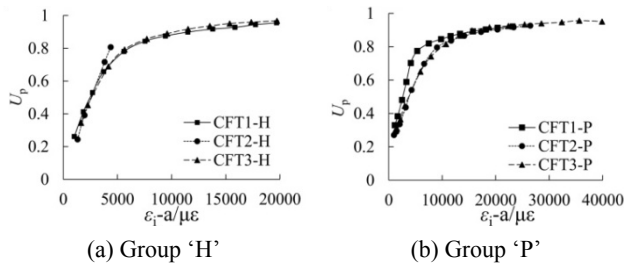


Fig. 9 Relative residual deformation ‘ $U_p$ ’- average strain ‘ $\epsilon_r-a$ ’ curves

Table 4 Tested characteristic relative residual deformation

Specimens	$U_p$			Test stop
	$\epsilon_y$	$2\epsilon_y$	$3\epsilon_y$	
CFT1-H	0.335	0.529	0.715	0.898
CFT2-H	0.274	0.548	0.789	0.807
CFT3-H	0.339	0.570	0.723	0.917
CFT1-P	0.398	0.633	0.776	0.922
CFT2-P	0.318	0.481	0.617	0.926
CFT3-P	0.331	0.490	0.615	0.951

\*Note:  $\epsilon_y$  is yield strain of external steel tubes; for group ‘H’ specimens  $\epsilon_y = 1434 \mu\epsilon$ , for group ‘P’ specimens  $\epsilon_y = 1811 \mu\epsilon$

residual deformation values corresponding to characteristic average strains are listed in Table 4.

From Fig. 9 and Table 4, it can be known that, the ‘ $U_p-(\epsilon_r-a)$ ’ curves of CFT1-H, CFT3-H are similar and the development of relative residual deformation presents a tendency of being firstly fast and then slow. Because the yielding and damage process of CFT2-H develops quickly, its ‘ $U_p-(\epsilon_r-a)$ ’ curve doesn’t have smooth developing stage; when the average strain exceeds two times of yield strain, the developing speed of relative residual deformation is faster than those of CFT1-H and CFT3-H. The ‘ $U_p-(\epsilon_r-a)$ ’ curves of CFT2-P, CFT3-P are similar. Compared with CFT2-P, CFT3-P, the relative residual deformation of CFT1-P develops quickly in the stage of the average strain from yielding to 15000  $\mu\epsilon$ , which shows that cavity construction benefits in putting off development of residual deformation.

Contrastive analysis. (1) Concrete strength doesn’t result in significant influence on the relative residual deformation, and only has some effect in the late deformation stage. (2) For group ‘H’ specimens, arrangement of reinforcement can effectively delay development of residual deformation, while for group ‘P’ specimens, the influence is far from obvious, which indicates that under low steel plate ratio, increasing the reinforcement ratio can improve residual deformation behavior. (3) Through comparison group ‘P’ specimens with group ‘H’ specimens, under the same multiple of yield strain, the residual deformation of the group ‘P’ specimens is smaller, which shows that the development of the residual deformation may be put off to some degree by increasing steel plate ratio.

### 3.4 Compressive stiffness

Based on the tested axial load ‘ $F$ ’- average strain ‘ $\epsilon_r-a$ ’ skeleton curves, the related secant stiffness ‘ $K$ ’- average strain ‘ $\epsilon_r-a$ ’ curves are shown in Fig. 10.

It can be known from Fig. 10 that the degrading process of compressive stiffness along with increase of average strain can be classified to three stages, including quick

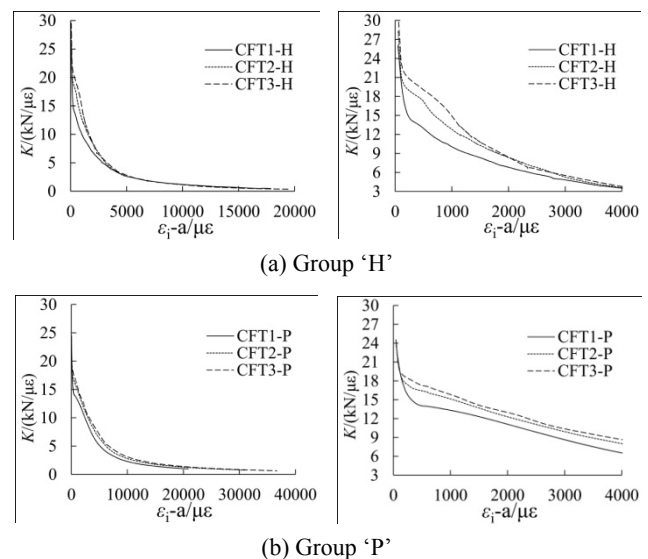


Fig. 10 Secant stiffness ‘ $K$ ’- average strain ‘ $\epsilon_r-a$ ’ curves

degrading stage, secondary quick degrading stage, and slow degrading stage. When the average strain is loaded to about  $150 \mu\epsilon$ , the test devices work at reliable accuracy and the tested stiffness differs from each other within a narrow range. At this time, the stiffness degradation goes into the quick degrading stage. When the average strain is loaded to reach two times of yield strain for group ‘H’ specimens and three times of yield strain for group ‘P’ specimens, the stiffness degradation slows down and goes into the secondary quick degrading stage. When the average strain is loaded to reach four times of yield strain for group ‘H’ specimens and eight times of yield strain for group ‘P’ specimens, the stiffness degradation speed is very slow and goes into the slow degrading stage.

Contrastive analysis. (1) In the quick degrading stage, the stiffness of CFT2-H, CFT3-H is higher than that of specimen CFT1-H; but in the secondary quick degrading stage and slow degrading stage, the stiffness of the three specimens tends to be very similar. However, specimens CFT2-P, CFT3-P have higher stiffness than specimen CFT1-P in all stages. (2) Compared with group ‘H’ specimens, the average strain values of the division points of group ‘P’ specimens are larger and the degrading speed is lower in the three stages. In conclusion, arrangement of reinforcement in cavities can lead to enhancement of stiffness, but under the situation of high steel plate ratio and low reinforcement ratio, the contribution of reinforcement is small; increase of concrete strength and cavity construction can slow down stiffness degradation.

### 3.5 Strain

The comparison between curves of axial load ‘ $F$ ’-average strain ‘ $\epsilon_t$ -a’ converted by displacement and curves of axial load ‘ $F$ ’- tested strain ‘ $\epsilon_t$ -m’ ( $m = 1, 2, 3, \dots$ ) measured by strain gages, and related skeleton curves for specimen CFT1-H and CFT2-P are shown in Fig. 11. In Fig. 11, the ‘Yielding’ vertical imaginary line represents the yield strain of steel plate of external steel tube.

From Fig. 11, it can be known that the development

trend of the tested strain versus axial load is similar with that of the converted average strain for specimen CFT1-H and CFT2-P. And other specimens show same trend as for similar cross section construction details. At early and middle stage of the ‘ $F$ - $\epsilon$ ’ curves, the values between the tested stain and converted average strain are close; while at late stage, the values of the tested strain are mostly smaller than the converted average strain, due to load transformation from external tube steel plates to core concrete and inner steel plates after local buckling. In addition, it can be known that when the specimens are loaded to reach ultimate bearing capacity, most of steel plates yield. Base on above results, in the later bearing capacity calculation, the real strain (or the tested strain) can be replaced by the converted average strain to simplify the calculation method.

### 4. Bearing capacity calculation

General assumption. (1) In bearing capacity calculation, tested values of concrete and steel strength are used. Due to the fact that concrete strength is evaluated by prismatic compressive strength in China while by cylinder strength in Japan, America and European, related conversion is carried out. (2) Material partial factor, axial compressive stability coefficient, and bearing capacity reduction factor resulting from concrete creep and accidental eccentricity are all excluded in bearing capacity calculation. (3) The external steel tubes are all arranged with studs or stiffen ribs, so the co-operative working performance between concrete and steel tubes can be guaranteed. (4) In order to simplify calculation using method in current specifications, the external steel tube, inner cavity steel plates, vertical stiffen ribs and reinforcements are converted to steel tube with equal area. In the conversion, due to the fact that the rectangular holes on latticed steel plates are relative small and the confinement effect to concrete can’t be neglected, the latticed steel plate cross section area is converted to a solid steel plate area according to the principle of equal volume steel ratio.

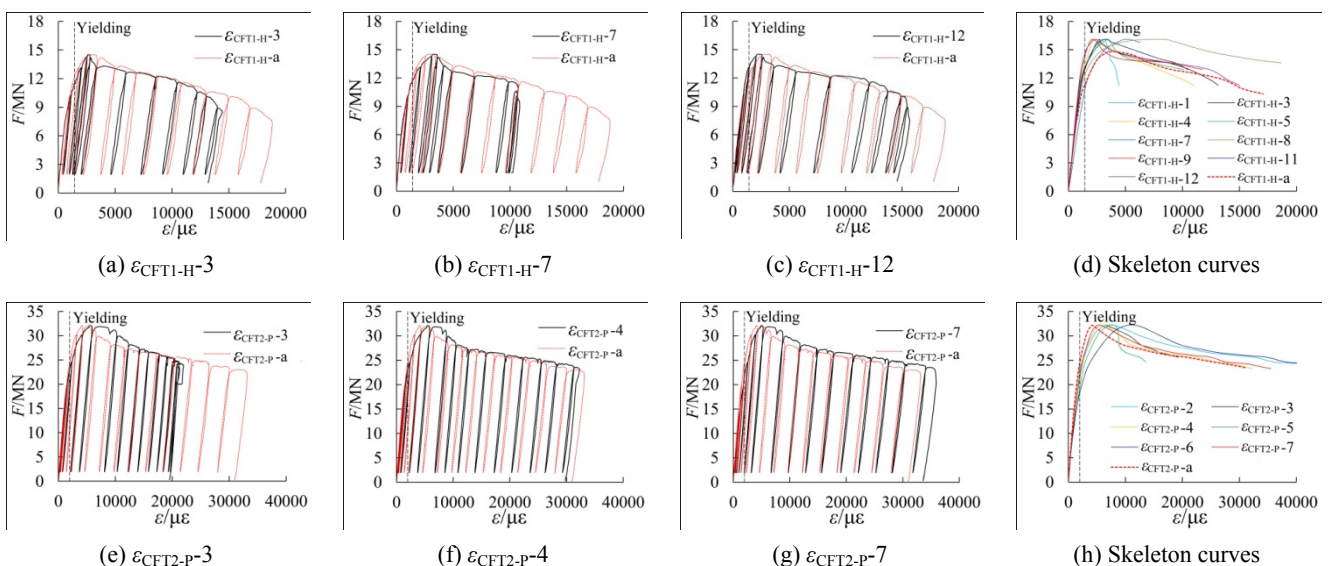
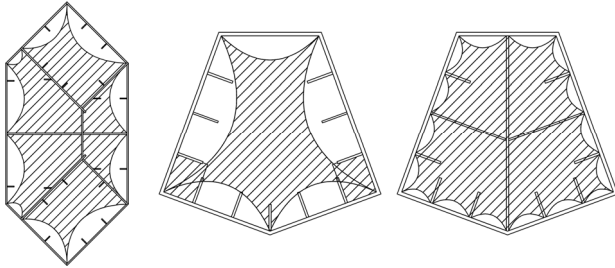


Fig. 11 Comparison between ‘ $\epsilon_t$ -m’ and ‘ $\epsilon_t$ -a’

Table 5 Influence coefficients of cross section shapes

Section shape	C	D
Round	$0.176 \bar{f}_y / 213 + 0.974$	$-0.104 f_{c,m} / 14.4 + 0.031$
Regular Octagon	$0.140 \bar{f}_y / 213 + 0.778$	$-0.070 f_{c,m} / 14.4 + 0.026$
Square	$0.131 \bar{f}_y / 213 + 0.723$	$-0.070 f_{c,m} / 14.4 + 0.026$



(a) CFT1-H ~ CFT3-H      (b) CFT1-P      (c) CFT2-P, CFT3-P

Fig. 12 Schematic diagram of active confined concrete

#### 4.1 Calculation methods in current specifications

##### 4.1.1 GB 50936 and CECS 254

The calculation method in GB 50936 and CECS 254 specification is as follows:

Composite strength

$$f_{sc} = (1.212 + C\xi + D\xi^2) f_{c,m} \quad (1)$$

In which, 'C' and 'D' are influence coefficients of cross section shape, listed in Table 5.

Axial compressive bearing capacity

$$F_{uc} = A f_{sc} \quad (2)$$

The calculated results of the six specimens by round, regular octagon and square CFT columns Eqs. (1)~(2) are shown in Fig. 13(a).

##### 4.1.2 ACI-318 and Eurocode 4

The calculation method in ACI-318 code is as follows

$$\phi F_{uc} = 0.85 \phi [0.85 f_{c,m} (A - A_s) + \bar{f}_y A_s] \quad (3)$$

In which,  $\phi = 1.0$  and the former 0.85 is influence coefficient of accidental eccentricity, but in this paper it would be 1.0;  $A_s$  is the whole area of steel plates and reinforcements.

The calculation method in Eurocode 4 is as follows

$$F_{uc} = A_{s1} f_{y1} + A_c f_{c,m} + A_{s2} f_{y2} \quad (4)$$

The calculated results of the six specimens are shown in Fig. 13(b).

##### 4.1.3 AISC-LRFD

The calculation method in AISC-LRFD specification is as follows

$$F_{uc} = \sigma_{cr} A_s \quad (5)$$

$$\sigma_{cr} = \begin{cases} (0.658^{\lambda_c^2}) f_{my} & (\lambda_c \leq 1.5) \\ (0.877 / \lambda_c^2) f_{my} & (\lambda_c > 1.5) \end{cases} \quad (6)$$

$$\lambda_c = \frac{kL}{r\pi} \sqrt{\frac{f_{my}}{E_m}} \quad (7)$$

$$f_{my} = \bar{f}_y + 0.85 f_{c,m} \left( \frac{A_c}{A_s} \right) \quad (8)$$

$$E_m = E_s + 0.4 E_c \left( \frac{A_c}{A_s} \right) \quad (9)$$

In Eqs. (5)~(9),  $k$  is effective length factor;  $L$  is laterally unbraced length;  $r$  is governing radius of gyration about the axis of buckling.

The calculated results of the six specimens are shown in Fig. 13(c).

##### 4.1.4 CECS 159 and AIJ

The calculation method in CECS 159 specification is as follows

$$F_{uc} = \bar{f}_y A_s + f_c A_{c,m} \quad (10)$$

The calculation method in AIJ standard is as follows

$$F_{uc} = \begin{cases} 1.27 f A_s + 0.85 f_{c,m} A_c & \text{round steel tube} \\ f A_s + 0.85 f_{c,m} A_c & \text{square steel tube} \end{cases} \quad (11)$$

In which  $f = \min(\bar{f}_y, 0.7 f_u)$ .

The calculated results of the six specimens are shown in Fig. 13(d).

#### 4.2 Calculation method in this paper

The confinement effect of irregular special-shaped CFT is lower than that of round CFT. The confinement effect is strong at the corner while weak at the center of straight side. Therefore, in this paper the polygonal core concrete is divided into active confined regions and inactive confined regions to reflect the confinement feature. Then an equivalent confinement reduction coefficient ' $k_e$ ' is adopted to reduce the confinement effect ' $\xi$ '; in this way the non-uniform confinement force is converted to uniform confinement force distributed along the steel tube wall. Finally, by quoting bearing capacity Eqs. (1)~(2) of round CFT columns, the bearing capacity of the specimens is calculated.

Zha's *et al.* (2010) research showed that the boundaries between active confined regions and inactive confined regions are parabola whose initial tangent angles can be assumed as 45 degrees. The expression of the boundary is as Eq. (12). Considering the confinement effect of cavity partition steel plate and stiffening ribs, the division of active confined concrete (dash region) and inactive confined concrete are shown in Fig. 12.

Table 6 Calculated results by method in this paper

Specimens	$k_e$	$\xi_{eq}$	C	D	$f_{sc}$	$F_{uc}$	$F_{uc}/F_u$
CFT1-H	0.699	0.662	1.222	-0.137	45.71	14311	0.967
CFT2-H	0.702	0.416	1.218	-0.199	53.71	16817	0.967
CFT3-H	0.699	0.484	1.222	-0.199	56.02	17540	0.999
CFT1-P	0.537	0.567	1.287	-0.250	72.30	25594	0.976
CFT2-P	0.856	1.110	1.293	-0.250	90.89	32176	1.002
CFT3-P	0.856	1.141	1.293	-0.250	91.76	32483	0.970

$$y = (-1/b)x^2 + b/4 \tag{12}$$

In which, 'b' is the length of side.  
The equivalent confinement coefficient

$$\xi_{eq} = k_e \xi \tag{13}$$

$$k_e = \frac{A_{ce}}{A_c} \tag{14}$$

Where,  $A_{ce}$  is the area of active confined concrete.

Based on above methods, the calculated results of the six specimens are listed in Table 6 and shown in Fig. 13(e).

### 4.3 Comparison of calculated results

The bearing capacity comparison between tested values

and calculated values gained by above methods based on different theories are shown in Fig. 13. In the figure, the horizontal coordinate stands for tested values, while the vertical coordinate stands for calculated values; the 45 degrees solid line stands for  $F_{uc} = F_u$ , and the dashed line stand for  $F_{uc}$  either 10% higher or lower than  $F_u$ .

It can be seen from above bearing capacity calculation equations and Fig. 13 that, (1) With reduction coefficient being excluded, besides the equations in GB50936, CECS254, AISC-LRFD and this paper, the bearing capacity equations in other specifications tend to be similar in form, and the main difference lies in the strength of concrete and steel. However, even though the equations are the same, the bearing capacity calculated by Chinese specifications is the lowest. (2) According to the round and octagon equations in GB50936 and CECS254 specifications, the calculated values are all greater than those of the tested values. However, according to the square equation, the calculated values are mostly lower than the tested values. (3) The calculated values of specimen CFT1-P according to methods in current specifications are much greater than other specimens. The reason may be that the confinement effect of CFT1-P is relatively weak due to only one cavity. (4) Most of values calculated by equations except for round equations are lower than tested values by 10%~25%; it shows that bearing capacity estimation of special-shaped CFT columns coupled with multiple cavities by current unified equations or square CFT columns equations is safe. (5) According to the method proposed in this paper, the relative error is within 5% for all specimens and the

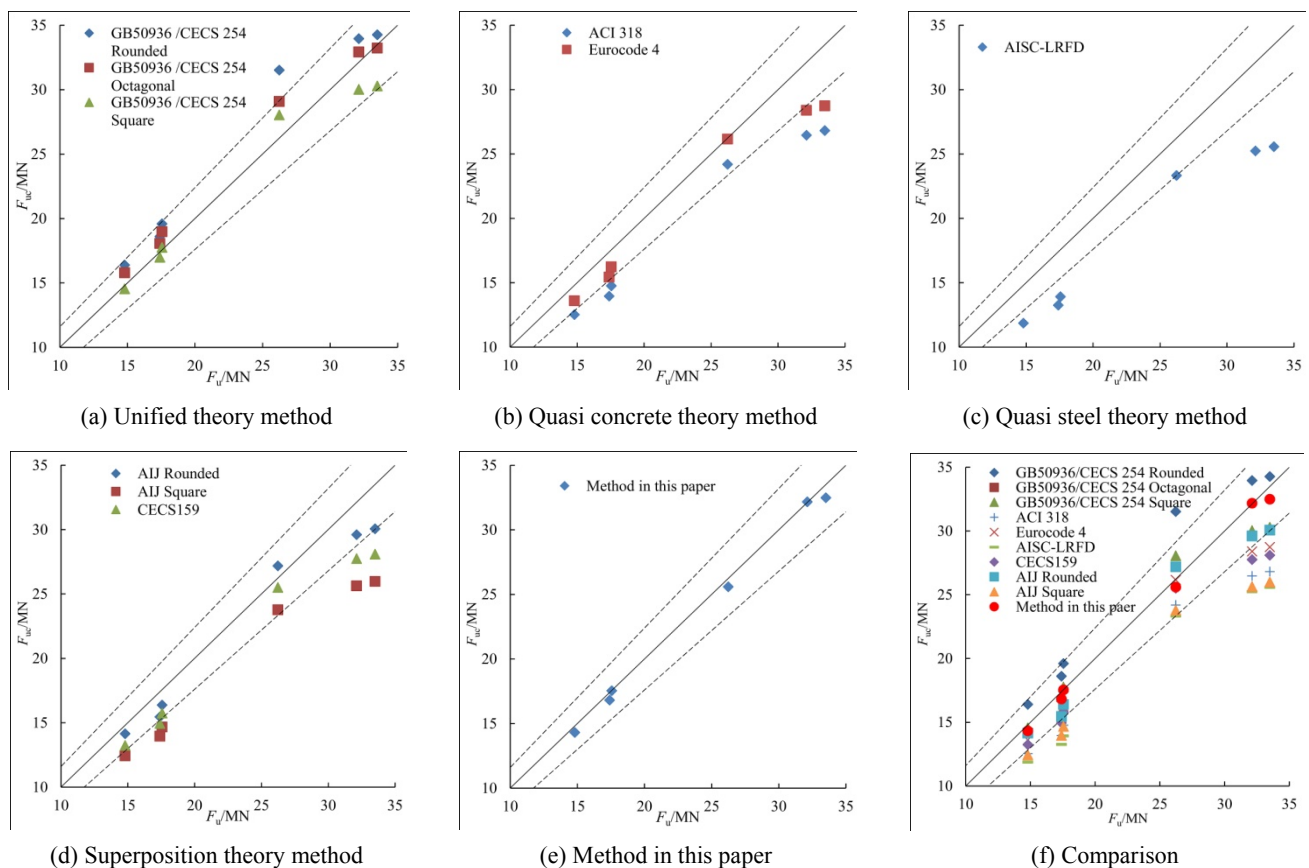


Fig. 13 Calculated bearing capacity comparison

accuracy of predicting specimen CFT1-P is higher than other methods; it shows that the method of dividing concrete into active and inactive confined regions is most useful and effective for bearing capacity prediction of special-shaped CFT columns with multiple cavities or not. (6) The proposed method has good cross section shape adaptability. However, more experimental verification is needed for other kinds of special-shaped CFT columns. So the proposal methods only can be used for the special-shaped CFT columns with similar cross sections in this paper.

### 5. Numerical simulation

#### 5.1 Finite element method (FEM) analysis model

FEM analysis software ABAQUS 6.14 is used to simulate the axial compressive behavior of all the six specimens. A basic FEM analysis mainly includes material model, 3-D model, element type, interaction defining, boundary, mesh, solving and so on.

Material model. A ‘Damaged Plasticity’ model is applied to simulate the concrete, while a ‘Plasticity’ model is applied to simulate the steel tube and reinforcement.

Element type. An 8-node linear brick, reduced integration, hourglass control, (C3D8R) element is used for concrete and loading block. A 4-node doubly curved thin shell, reduced integration, hourglass control, finite membrane strains, (S4R) element is used for multi-cavity steel tubes, including external steel tubes, partition steel plates, and stiffening ribs. A 2-node linear 3-D truss, (T3D2) element is used for reinforcement.

3-D model. In order to make it easy to apply axial load, elastic loading blocks are arranged at upper and lower ends of the columns. Even though the concrete is poured in several cavities in test, in FEM analysis model the concrete is established into a whole polygonal prism whose shape is the same with the external steel tube to simplify calculation. Because if in actual way, there tend to be too many contact pairs, and the calculation amount is very complex due to high nonlinearity. As a result, convergence may be difficult. The influence of this difference is assessed by material constitutive relation in later section.

Interaction defining. The interaction including contact

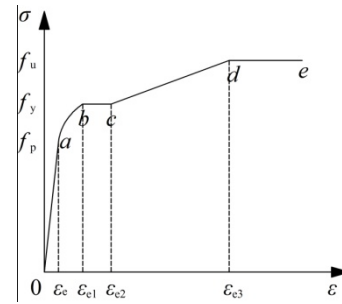


Fig. 15 ‘ $\sigma_s$ - $\epsilon_s$ ’ curve of steel

pairs and constraint pairs among steel tube, concrete prism, reinforcement and loading block. The behavior of contact pairs between steel tube and concrete prism is divided into a ‘Hard Contact’ in normal direction and a ‘Coulomb Friction’ in tangential direction. The friction coefficient is 0.2 as per Baltay and Gjelsvik (1990). The constraint pairs between steel tube and loading block are ‘Tie’, so are the constraint pairs between concrete prism and loading block. The reinforcements are all ‘embedded’ in the concrete. The upside of upper loading block is constrained by a reference point with ‘Continuum distributing coupling’.

Boundary. A ‘Pinned ( $U_1 = U_2 = U_3 = 0$ )’ boundary is used at the downside of lower loading block. And a ‘Displacement ( $U_1 = 0, U_2 = 0, U_3 = \Delta$ )’ boundary is used at the reference point to apply axial load.

Mesh. A ‘Structured’ mesh technology is used for concrete prism and loading block. And a ‘Sweep’ mesh technology based on ‘Advancing front’ algorithm is used for steel tube.

Base on above method, the established meshed FEM analysis model is shown in Fig. 14.

#### 5.2 Material constitutive relation

##### 5.2.1 Steel

The steel tubes and reinforcements all belong common low-carbon soft steel materials. The stress ‘ $\sigma_s$ ’-strain ‘ $\epsilon_s$ ’ curves can be divided into five stages, shown in Fig. 15. And the equations of the curves are listed as follows. Taking the tested values of yield stress and elasticity modulus into Eq. (15), the discrete ‘ $\sigma_s$ - $\epsilon_s$ ’ points are inputted into ABAQUS software.

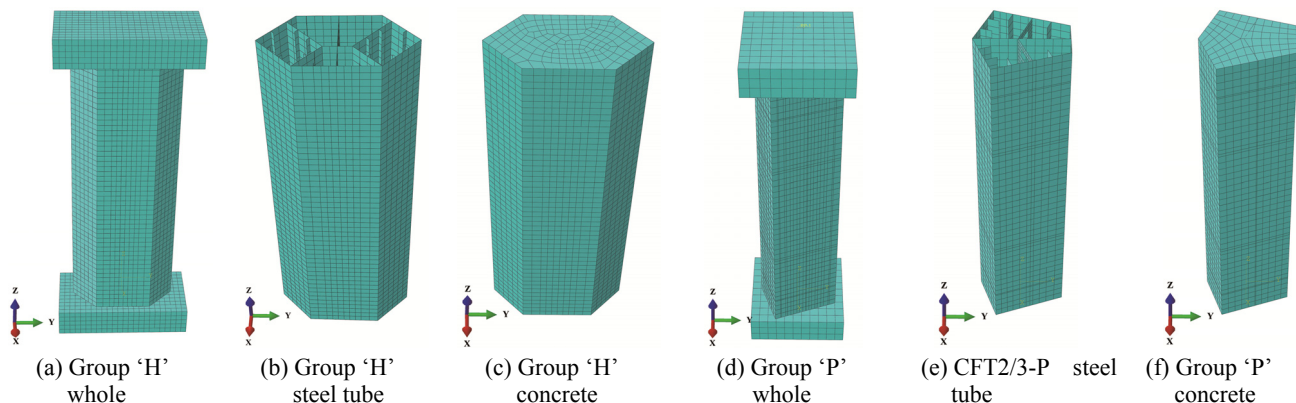


Fig. 14 Meshed FEM analysis model

$$\sigma_s = \begin{cases} E_s \varepsilon_s, & \varepsilon_s \leq \varepsilon_e \\ -U \varepsilon_s^2 + V \varepsilon_s + W, & \varepsilon_e \leq \varepsilon_s \leq \varepsilon_{e1} \\ f_y, & \varepsilon_{e1} \leq \varepsilon_s \leq \varepsilon_{e2} \\ f_y \left[ 1 + 0.6 \frac{\varepsilon_s - \varepsilon_{e2}}{\varepsilon_{e3} - \varepsilon_{e2}} \right], & \varepsilon_{e2} \leq \varepsilon_s \leq \varepsilon_{e3} \\ 1.6 f_y, & \varepsilon_s > \varepsilon_{e3} \end{cases} \quad (15)$$

In which,  $\varepsilon_e = 0.8f_y/E_s$ ,  $\varepsilon_{e1} = 1.5\varepsilon_e$ ,  $\varepsilon_{e2} = 10\varepsilon_{e1}$ ,  $\varepsilon_{e3} = 100\varepsilon_{e1}$ ,  $U = 0.2f_y/(\varepsilon_{e1}-\varepsilon_e)^2$ ,  $V = 2U\varepsilon_{e1}$ , and  $W = 0.8f_y + U\varepsilon_{e2} - V\varepsilon_e$ .

### 5.2.2 Concrete

The behavior of steel tube confined concrete is very different from that of normal concrete. It is characterized by increase of strength and plastic deformation. In ABAQUS software, the strength increase of concrete due to the confinement effect of steel tube can be implemented by inputting parameters to define yield surface. But the plastic behavior increase only can be reflected in stress ‘ $\sigma_c$ ’- strain ‘ $\varepsilon_c$ ’ curves. Han’s (2008) ‘ $\sigma_c$ - $\varepsilon_c$ ’ equations suitable for FEM analysis of square CFT column are used in this paper. The equations are as follows

$$y = \begin{cases} 2x - x^2 & (x \leq 1) \\ \frac{x}{\beta_0(x-1)^\eta + x} & (x > 1) \end{cases} \quad (16)$$

In which,  $x = \frac{\sigma_c}{\sigma_0}$ ,  $y = \frac{\varepsilon_c}{\varepsilon_0}$ ,  $\sigma_0 = f_{c,m}$ ,  $\varepsilon_0 = \varepsilon_c + 800\xi^{0.2}$ .

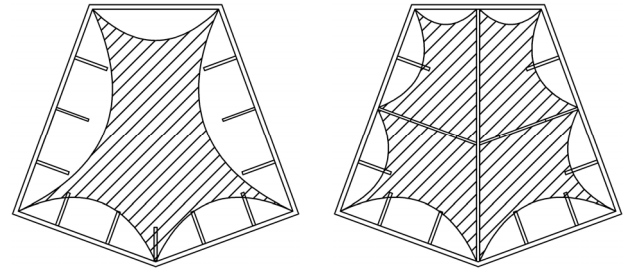
$10^{-6}$ ,  $\eta = 1.6 + 1.5/x$ ,  $\beta_0 = \frac{(f_{c,m})^{0.1}}{1.2\sqrt{1+\xi}}$ ,  $\varepsilon_c = \left( 1300 - \right.$

$\left. + 12.5f_{c,m} + \left[ 1330 + 760 \left( \frac{f_{c,m}}{24} - 1 \right) \right] \mu^{0.2} \right) \cdot 10^{-6}$ , and  $\mu$  is

Poisson’s ratio.

Due to the fact that the concrete is established into a whole polygonal prism in FEM analysis models instead of several polygonal prism in separate cavities, the beneficial confinement effect of cavity partition steel plate is ignored for some specimens; and this may result in errors. So a method of increasing concrete strength by theoretical calculation in Section 4.2 is applied to reflect the beneficial effect.

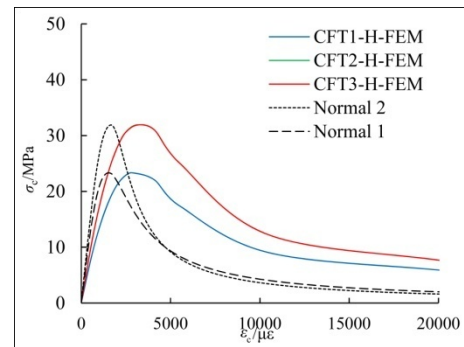
The beneficial effect of cavity partition steel plates lies in dividing concrete into active and inactive confined regions in theoretical analysis. From Fig. 12, it can be known that the cavity partition steel plates and vertical stiffening ribs play significant roles in the division. Due to the fact that the partition steel plates can effectively confine external steel tube in FEM analysis model, so their role is considered in simulation. Now, only the role of vertical stiffening ribs is not considered. Also from Fig. 12, it can be known that if the vertical stiffening ribs are too weak in one cavity (qualitatively judged by area ratio, arrangement location and so on), it may not be able to confine the



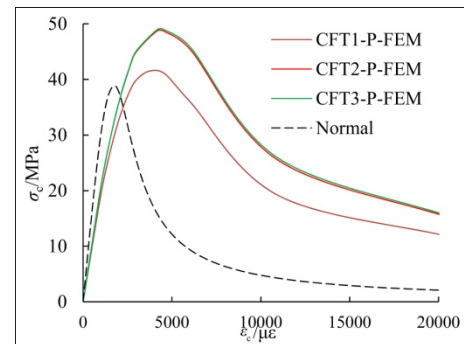
(a) CFT1-P-FEM (b) CFT2-P-FEM CFT3-P-FEM  
Fig. 16 Division of concrete confined region in FEM analysis model case

Table 7 Increased concrete strength in FEM analysis model

Specimens	CFT1-H-FEM ~CFT3-H-FEM	CFT1-P -FEM	CFT2-P -FEM	CFT3-P -FEM
$k_c$	—	0.479	0.643	0.643
$\Delta\sigma_c/\text{MPa}$	0	2.64	9.80	10.07



(a) Group ‘H’



(b) Group ‘P’

Fig. 17 ‘ $\sigma_c$ - $\varepsilon_c$ ’ curve of concrete

concrete effectively. So, for specimens CFT1-H~CFT3-H, the division of concrete in FEM analysis model case is the same as its actual model case, and the concrete strength needn’t be increased; but for specimens CFT1-P~CFT3-P, the division of concrete in FEM analysis model case is different, shown in Fig. 16. Based on the bearing capacity calculation method in Section 4.2, the only difference between CFT1-P-FEM and CFT1-P, CFT2-P-FEM and CFT2-P, CFT3-P-FEM and CFT3-P is the parameter ‘ $k_c$ ’.

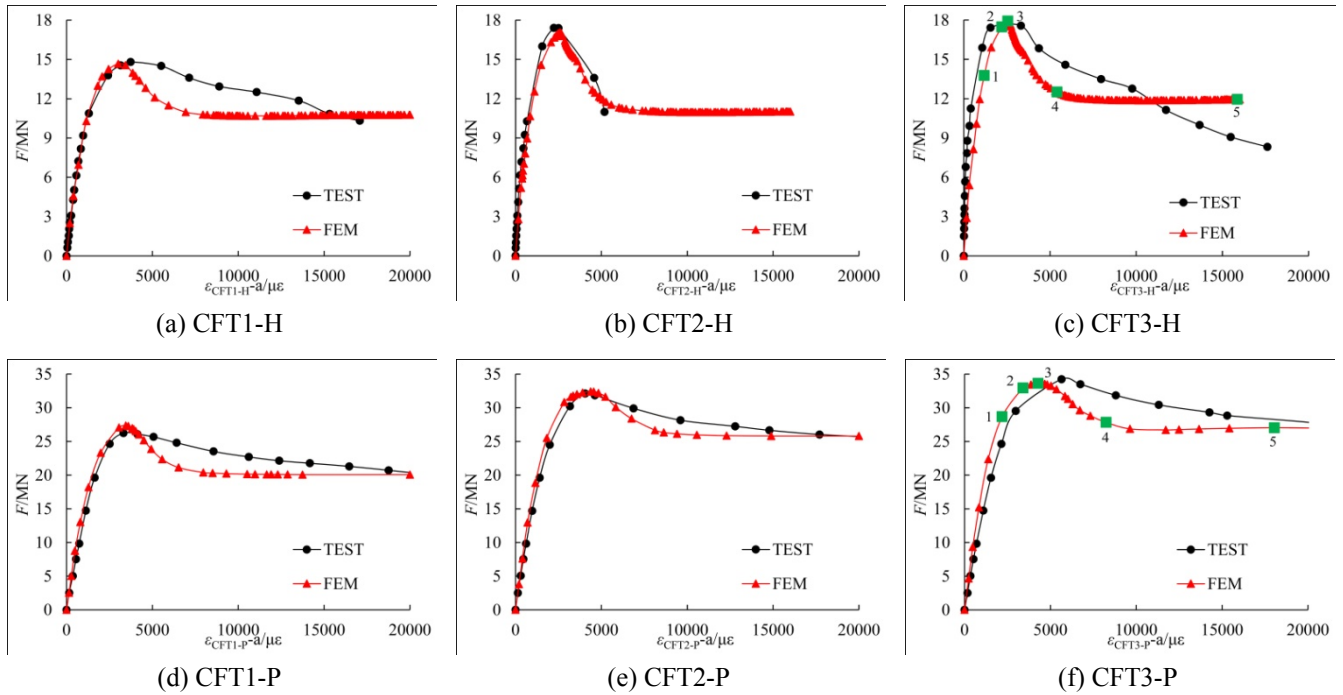


Fig.18 ‘F-(ε<sub>i</sub>-a)’ curves comparison between test results and FEM results

As a result, the increased value of concrete strength in FEM model is calculated by Eq. (17), and listed in Table 7. The inputted in ABAQUS concrete ‘σ<sub>c</sub>-ε<sub>c</sub>’ curves are showing in Fig. 17.

$$\Delta\sigma_c = \frac{F_{FEM} - F_{uc}}{A_c} \quad (17)$$

In which,  $F_{FEM}$  is the calculated bearing capacity of cross section in FEM analysis model.

### 5.3 FEM analysis results

#### 5.3.1 Comparison between simulation and test

A numerical simulation was carried out for the tested six

specimens according to above methods. The ‘F-(ε<sub>i</sub>-a)’ curves comparison between test results and FEM results are shown in Fig. 18. The simulated Mises stress and compressive Damage diagrams of specimens CFT3-H and CFT3-P when the average strain reaches about 10000 με are shown in Fig. 19.

From Fig. 18, it can be known that the simulated ‘F-(ε<sub>i</sub>-a)’ curves match the tested curves well. The simulated ascent branch is very accurate until peak point, but the descending branch is a little lower within limited errors. From Fig. 19, it can be known that when the specimens reach inelastic deformation stage, stress and damage develop along staggered direction for group ‘H’ specimens, while that along an approximately horizontal direction for

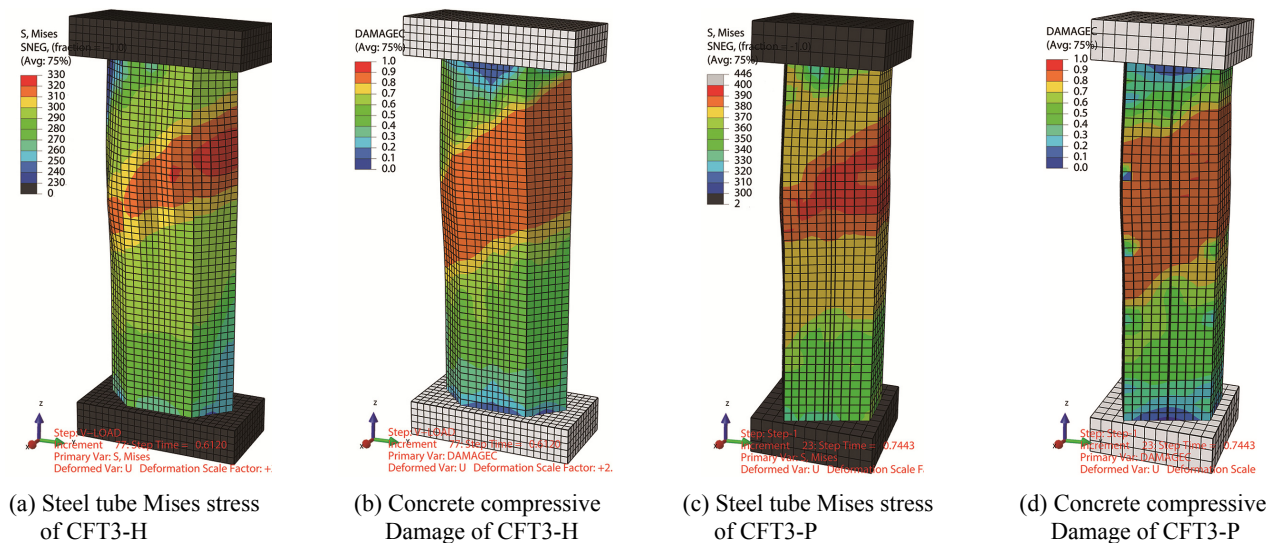


Fig. 19 Stress and damage diagram of specific specimens at 10000με

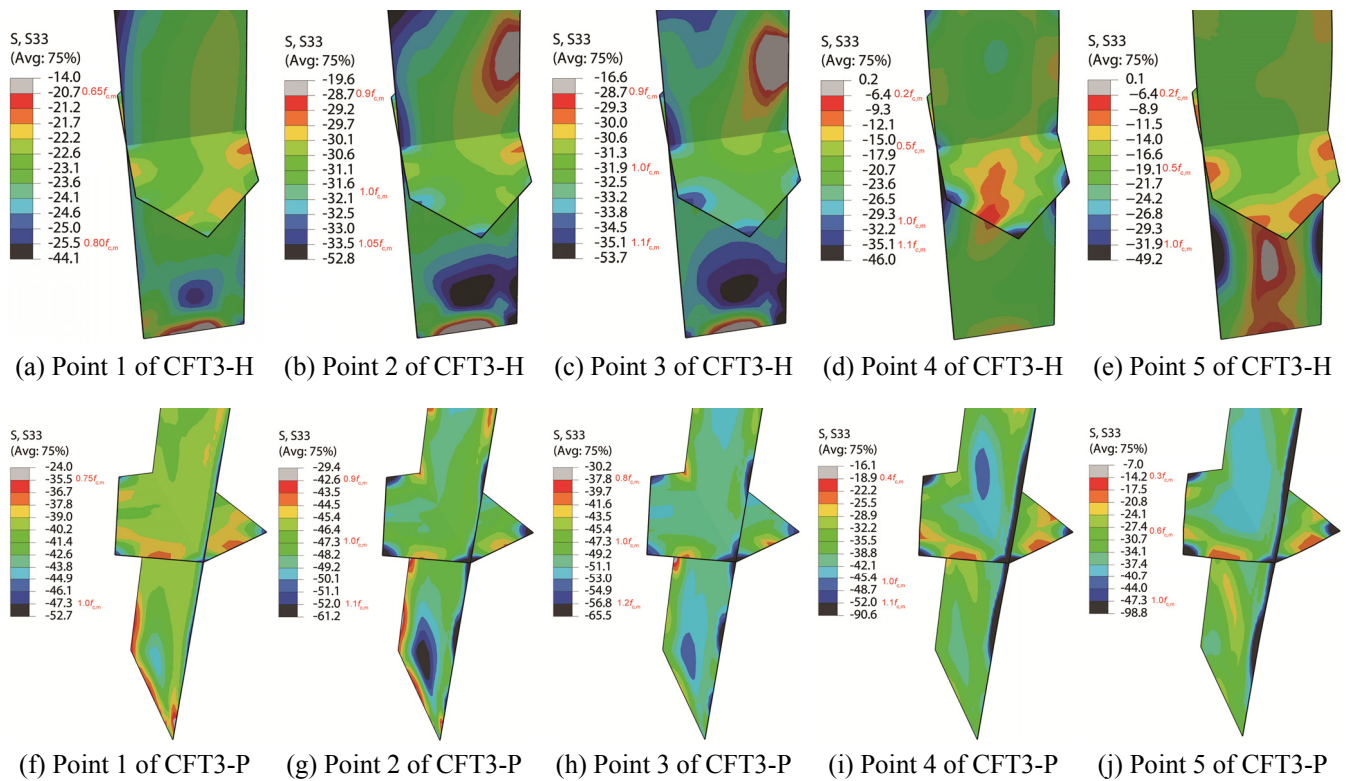


Fig.20 Vertical stress distribution results of confined concrete at different loading stages

group ‘P’ specimens, which matches the test phenomenon. All the results above indicate that the method of establishing the FEM model in this paper is right and reliable.

### 5.3.2 Stress distribution of concrete

The simulated vertical stress distribution results of confined concrete of specimens CFT3-H and CFT3-P at different feature points of ‘ $F-(\varepsilon_r-a)$ ’ curves in Figs. 18(c) and (f) are shown in Fig. 20. In the figures, the concrete is cut at horizontal and vertical axis of symmetry, in this way the vertical stress is partly shown on the horizontal and vertical plane of symmetry.

From Fig. 20, it can be known that, at the point 1, the stress of concrete at horizontal central cross section is near in some degree. At the point 2, the stress at corner is greater than other places and the values decline along with the increase of distance from the corner. When the specimens are loaded to ultimate bearing capacity (point 3), the stress at corner is still the greatest, while the stress at the center of straight sides is the lowest; moreover, the stress at the center of horizontal cross section is also relative greater than other places except for at the corner. Along with the increase of vertical strain, the stress at the corner and center declines, and the ‘ $F-(\varepsilon_r-a)$ ’ curves go into the descending branch. Due to the fact that the confinement effect of group ‘H’ specimens is more imbalanced than group ‘P’ specimens, the concrete stress of group ‘H’ specimens distributes in a slant way while that of group ‘P’ specimens are not. Based on above results, it may also illustrate that the method in section 4.2 of dividing concrete into active confined regions and inactive confined regions is relatively reasonable.

## 6. Conclusions

- In special-shaped CFT columns coupled with multiple cavities, multi-cavity construction and reinforcement in cavities form combined confinement to in-filled concrete; the bearing capacity, ductility, energy dissipation ability and residual deformation are all improved significantly.
- Compared with the hexagonal specimens, the steel ratio of the pentagonal specimens is higher and the moment of inertia of cross section is more balanced. Therefore, the descending branch of the tested load-average strain curves is smooth and the working performance is relatively stable; it is beneficial in fully playing the role of dissipating earthquake energy in elastic-plastic deformation process.
- The bearing capacity of special-shaped CFT columns coupled with multiple cavities calculated by equations except for round CFT columns equations in current specifications are lower than the true values.
- The proposed method of dividing concrete into active and inactive confined regions is accurate for the axial compressive bearing capacity prediction of special-shaped CFT columns coupled with multiple cavities or not. In addition, its only can be applied in CFT columns with similar cross section in this paper due to a lack of more experimental verification.
- The simplified method of establishing FEM analysis model is reliable and accurate for the elastic-plastic compressive behavior prediction of special-shaped CFT columns coupled with multiple cavities.

Moreover, the provided constitutive relation of confined concrete is also suitable.

## Acknowledgments

The research described in this paper was financially supported by the National Natural Science Foundation of China under Grant No. 51408017.

## References

- ACI 318 (2011), Building code requirement for structural concrete and commentary; American Concrete Institute, Farmington Hills, MI, USA.
- AIJ (2001), Standard for structure calculation of steel reinforced concrete structures, Architectural Institute of Japan; Tokyo, Japan.
- AISC-LRFD (1999), Load and resistance factor design specification; American Institute of Steel Construction, Chicago, USA.
- Baltay, P. and Gjelsvik, A. (1990), "Coefficient of friction for steel on concrete at high normal stress", *J. Mater. Civil Eng.*, **2**(1), 46-49.
- BS EN 1994-1-1 (2004), Eurocode 4: Design of composite steel and concrete structures – part 1-1: general rules for buildings; British Standard Institution, London, UK.
- CECS 159 (2004), Technical specification for structures with concrete-filled rectangular steel tube members; China Association for Engineering Construction Standardization, Beijing, China.
- CECS 254 (2012), Technical specification for solid and hollow concrete-filled steel tubular structure; China Association for Engineering Construction Standardization, Beijing, China.
- Chithira, K. and Baskar, K. (2014), "Experimental study on circular concrete filled steel tubes with and without shear connectors", *Steel Compos. Struct., Int. J.*, **16**(1), 99-116.
- Du, G.F., Song, X. and Yu, S.P. (2013), "Experimental research on axially loaded composite L-section steel tubular short columns filled with steel-reinforced concrete", *J. Build. Struct.*, **34**(8), 82-89.
- GB/T 50081 (2011), Standard for test method of mechanical properties on ordinary concrete; Standards Press of China, Beijing, China.
- GB/T 228.1 (2010), Metallic materials - Tensile testing - Part 1: method of test at room temperature; Standard Press of China, Beijing, China.
- GB 50936 (2014), Technical code for concrete filled steel tubular structures; China Architecture & Building Press, Beijing, China.
- Guo, Z.H. and Shi, X.D. (2015), *Reinforced Concrete Theory and Analyse*, (3rd Edition), Tsinghua University Press, Beijing, China.
- Gupta, P.K., Verma, V.K. and Khaudhair, Z.A. (2015), "Effect of tube area on the behavior of concrete filled tubular columns", *Comput. Concrete, Int. J.*, **15**(2), 141-166.
- Han, L.H., Liu, W. and Yang, Y.F. (2008), "Behaviour of concrete-filled steel tubular stub columns subjected to axially local compression", *J. Constr. Steel Res.*, **64**(4), 377-387.
- Hua, W., Wang, H.J. and Hasegawa, A. (2014), "Experimental study on reinforced concrete filled circular steel tubular columns", *Steel Compos. Struct., Int. J.*, **17**(4), 517-533.
- Jamaluddin, N., Lam, D. and Dai, X.H. (2013), "An experimental study on elliptical concrete filled columns under axial compression", *J. Constr. Steel Res.*, **87**, 6-16.
- Kim, H.S. and Kang, J.W. (2012), "An efficient structural analysis of super tall mega frame buildings using a multi-level condensation method", *J. Asian Architect. Build. Eng.*, **11**(2), 343-350.
- Lee, D., Ha, T. and Jung, M. (2014), "Evaluating high performance steel tube-framed diagrid for high-rise buildings", *Steel Compos. Struct., Int. J.*, **16**(3), 289-303.
- Li, X.P. and Lu, X.L. (2008), "Modelling and experimental verification on concrete-filled steel tubular columns with T or L section", *Progress Steel Build. Struct.*, **10**(4), 56-62.
- Li, G.C., Yang, Z.J., Lang, Y. and Fang, C. (2016), "Behavior of CFST columns with inner CFRP tube under biaxial eccentric loading", *Steel Compos. Struct., Int. J.*, **22**(6), 1487-1505.
- Liu, P., Yin, C. and Li, X. (2012), "Structural system design and study of Tianjin Goldin 117 mega tower", *Build. Struct.*, **43**(3), 1-9.
- Qian, J.R., Zhang, Y. and Ji, X.D. (2011), "Test and analysis of axial compressive behavior of short composite-sectioned high strength concrete filled steel tubular columns", *J. Build. Struct.*, **32**(12), 162-169.
- Shen, Z.Y., Lei, M. and Li, Y.Q. (2013), "Experimental study on seismic behavior of concrete-filled L-shaped steel tube columns", *Adv. Struct. Eng.*, **16**(7), 1235-1247.
- Tu, Y.Q., Shen, Y.F. and Li, P. (2014), "Behaviour of multi-cell composite T-shaped concrete-filled steel tubular columns under axial compression", *Thin-Wall. Struct.*, **85**, 57-70.
- Wang, L.C., Wang, X.J. and Ji, D.H. (2012), "Structural design and analysis on Dalian Guomao Tower", *Build. Struct.*, **42**(2), 74-80.
- Zha, X.X., Li, Y.T. and Zhong, S.T. (2010), "Unified formula of Circular, polygonal, solid, hollow concrete filled steel tube columns under axial compression", *Proceedings of the 2010 National Symposium of Steel Structure*, Beijing, China, October.
- Zuo, Z.L., Cai, J. and Yang, C. (2012), "Axial load behavior of L-shaped CFT stub columns with binding bars", *Eng. Struct.*, **37**, 88-98.

CC